Soft Matter

PAPER

View Article Online
View Journal | View Issue

Cite this: *Soft Matter*, 2024, **20**, 3931

Significant anisotropic deformation and optical shifts in stretched cholesteric liquid crystal elastomers

Saki Mori,[a] Hideaki Takagi,[b] Nobutaka Shimizu,[b] Noriyuki Igarashi,[b]
Shinichi Sakurai[c] and Kenji Urayama *[d]

This study explores the opto-mechanical response of cholesteric liquid crystal elastomers (CLCEs) subjected to uniaxial stretching along the *x*-axis, perpendicular to their helical *z*-axis. A definitive crossover is observed in the strain (ε_x) dependencies of various optical and mechanical properties, such as the transmission spectra, degree of mesogen orientation, Poisson's ratios, and tensile stress. At low strains, CLCEs exhibit a blue shift in the selective reflection band due to a reduction in the helical pitch, accompanied by a decrease in reflection selectivity for circularly polarized light. Beyond a certain critical strain (ε_x'), further pitch alterations halt. This strain regime is marked by substantial anisotropic lateral contractions without any *z*-axis contraction, as indicated by a Poisson's ratio (μ_{xz}) of zero. Within this intermediate strain regime, local directors predominantly reorient towards the *x*-direction within the *xy*-plane, resulting in a quasi-plateau of tensile stress. Approaching a higher critical strain (ε_x''), a complete loss of reflective selectivity occurs. Past this threshold, while the mechanical responses resemble those of isotropic conventional rubber, they retain a periodic structure albeit without phase chirality. These observed features are accounted for by the Mao–Terentjev–Warner model, especially when the network anisotropy parameter is adjusted to match the critical strain magnitude (ε_x'') associated with the cessation of selective reflection.

Received 19th March 2024,
Accepted 17th April 2024

DOI: 10.1039/d4sm00325j

rsc.li/soft-matter-journal

1. Introduction

Cholesteric liquid crystals (CLCs) exhibit unique optical properties due to their helical director configurations with a pitch in the range of several hundred nanometers.[1,2] In particular, they exhibit the selective reflection of circularly polarized light that matches the handedness of the helix, with a wavelength that corresponds to the helical pitch. Cholesteric liquid crystal elastomers (CLCEs) combine the elasticity of rubber with the optical properties of CLCs.[3,4] The dual nature of CLCEs allows for the modulation of the optical behavior through external mechanical stimuli,[5–7] and for the deformation through temperature variation[3,8–10] and electric fields[11,12] affecting the director alignments. Specifically, applying strain to CLCE films and fibers has been shown to significantly alter their optical traits, including shifts in the reflected color due to changes in the helical pitch prompted by macroscopic dimensional variations.[13,14] This strain-induced variation in optical properties for CLCE films was used for tunable lasing.[5,15–18] The mechanochromic response also allows for their use in tensile and pressure sensors with high spatial resolution.[13,14,19–22] These opto-mechanical features make CLCEs particularly interesting as tunable photonic soft materials.

CLCEs may undergo complex deformations depending on their geometries when employed as photonic materials. When the original helical axis is along the *z*-direction, uniaxial compression along this axis[15] or equal-biaxial stretching perpendicular to it[5,16] leads to a straightforward reduction in the helical pitch while preserving the initial orientation symmetry within the *xy* plane. In these cases, the reflection band exhibits a blue-shift proportionally to the dimensional change in the *z*-direction, and the reflection selectivity is retained even at high strains. Conversely, stretching along the axis perpendicular to the original helical axis complicates the opto-mechanical response due to the disruption of the initial orientation symmetry in the *xy* plane, resulting in the loss of reflection selectivity in many cases. Most of the previous studies have found that the variation in helical pitch with applied stretch λ_x is less than what isotropic contraction and affine

---

[a] *Department of Macromolecular Science and Engineering, Kyoto Institute of Technology, Kyoto, 606-8585, Japan*
[b] *High Energy Accelerator Research Organization, Tsukuba, Ibaraki 305-0801, Japan*
[c] *Department of Biobased Materials Science, Kyoto Institute of Technology, Kyoto, 606-8585, Japan*
[d] *Department of Material Chemistry, Kyoto University, Kyoto, 615-8510, Japan. E-mail: urayama.kenji.2s@kyoto-u.ac.jp*

displacement would predict,[6–8,17,18] while one study reported the agreement between them.[13] They have analyzed this behavior using a power law of $\Lambda_{\text{red}} = \lambda_x^{-\gamma}$, where Λ_{red} is the ratio of the characteristic wavelengths in deformed and undeformed states. When lateral contractions in the y- and z-directions are equal, and the helical pitch varies proportionally with the material's dimension, the γ value is 0.5. However, most of the previous studies have reported lower γ values in the early stage of stretching, suggesting that the helical configuration resists macroscopic contraction along the helical axis, with γ serving as an analogue to the Poisson's ratio under affine deformation assumptions. Nevertheless, the exact relationship between these microscopic and macroscopic deformations remains unclear due to the absence of direct measurements of Poisson's ratio. Understanding the λ_x dependence of Λ_{red} and its relationship with the Poisson's ratio will shed light on how these deformation scales are interconnected.

When CLCEs are sufficiently stretched, it is expected that their helical structure will unwind entirely. Previous studies have demonstrated the total loss of selective reflection at extensive elongations.[6–8,13,18] However, the details concerning how stretching influences the unwinding of the helical director configuration remain to be elucidated. This research aims to clarify the opto-mechanical response of main-chain type CLCEs synthesized through thiol–ene reactions. We examine CLCEs with different cross-link geometries—one with an explicit tetra-functional cross-linker and another without, because some studies reported that the flexibility, length and functionality of cross-linker molecules have pronounced effects on the orientation coupling between the mesogens and network backbone.[23–25] Our analysis discerns a three-stage strain response defined by two strain thresholds. We investigate changes in transmission spectra, Poisson's ratio, degree of mesogen orientation, and tensile stress in relation to stretching. Notably, for CLCEs with a tetra-functional cross-linker, we identify an intermediate strain regime where neither helical pitch variation nor macroscopic contraction along the z-axis occurs. During this strain regime, tensile stress remains nearly constant while there is significant rotation of local directors within the xy plane. Beyond this strain threshold, the material begins to exhibit characteristics akin to conventional isotropic rubber, including isotropic lateral contractions and an increase in stress. We demonstrate that the Mao–Terentjev–Warner model[26,27] captures the key phenomena observed in the experiments. These insights deepen our understanding of the complex interaction between LC alignment and macroscopic deformation in CLCEs, providing a foundation for harnessing and refining their opto-mechanical responses.

2. Experimental

2.1. Sample preparation

We prepared two types of main-chain CLCE films, designated as CLCE-0 and CLCE-4, with different cross-link geometries. These were prepared *via* a thiol–ene reaction.[28] The reactant mixtures comprise a liquid crystalline diacrylate, specifically

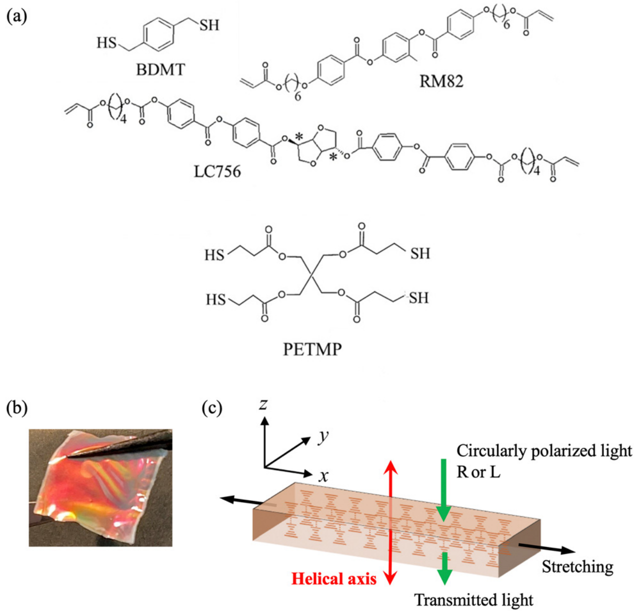

Fig. 1 (a) Chemical structures of BDMT, RM82, LC756 and PETMP. (b) Appearance of CLCE-0 with iridescent color. (c) Schematic diagram of experimental geometry.

1,4-bis[4-(6-acryloxypropoxy)benzoyloxy]-2-methylbenzene (RM82; Osaka Organic Chemical Industry), and a chiral diacrylate, 1,4:3,6-dianhydro-, 2,5-bis[4-[[4-[[[4-[(1-oxo-2-propen-1-yl)oxy]butoxy]carbonyl]oxy]benzoyl]oxy]benzoate] (LC756; BASF). Additionally, 1,4-benzenedimethanethiol (BDMT; Tokyo Chemical Industry) served as a chain extender. For the preparation of CLCE-4, we introduce an explicit tetrafunctional cross-linker, pentaerythritol tetrakis(3-mercaptopropionate) (PETMP; Tokyo Chemical Industry). The chemical structure of each reactant is shown in Fig. 1a. The compositions of each specimen are detailed in Table 1, and "*X*" in the sample code CLCE-*X* represents the molar ratio of PETMP to RM82. Bis(cyclopenta-2,4-dien-1-yl)bis[2,6-difluoro-3-(1*H*-pyrrol-1-yl)phenyl]titanium (Irgacure 784®) was used as the photoinitiator. The initiator solution (0.229 mol L^{-1}) using dichloromethane as a solvent was added to the reactant mixtures, and dried under vacuum conditions.

The melted reactant mixtures, heated to 110 °C, were loaded into a glass cell with a 30 μm gap. The cell surfaces had been previously coated with a uniaxially rubbed polyimide layer to induce planar orientation.[9,15] The glass cell was cooled at a rate of 0.5 °C min^{-1} to the cholesteric phase onset temperature (65 °C for CLCE-0 and 57 °C for CLCE-4). The cooling then proceeded at a reduced rate of 0.1 °C min^{-1} to a temperature 5 °C below the cholesteric–isotropic phase transition temperature for each

Table 1 Molar ratios of the constituent reactants, film thicknesses, and Young's modulus for CLCE-0 and CLCE-4

Specimen	RM82	LC756	BDMT	PETMP	Thickness (μm)	Young's modulus (MPa)
CLCE-0	1	0.036	1.08	0	28.5	5.8
CLCE-4	1	0.036	1.08	0.040	28.6	4.5

system, and the temperature was maintained for 24 hours. The formation of a monodomain cholesteric phase, with the helical axis perpendicular to the substrate, was confirmed by the appearance of iridescent color and oily streak textures, using a polarizing microscope. The glass cells were then exposed to light with a wavelength of 525 nm for 30 minutes to induce photopolymerization. After irradiation, the cells were immersed in dichloromethane, causing the resultant gel films to detach from the glass substrates due to swelling pressure. The detached gel films were subsequently allowed to deswell gradually by the stepwise addition of methanol to the solvent mixture. The final elastomer films with iridescent color as shown in Fig. 1b were obtained after drying the deswollen gels. Table 1 lists the thickness of each film specimen which was measured at 25 °C using a double-scan high-precision laser measuring instrument, LT-9010M (Keyence, Japan). The Young's modulus for each specimen listed in Table 1 was estimated from the initial slope of the stress–strain curve, which will be shown later. The two types of CLCE have comparable moduli, despite a difference in the amount of PETMP. This suggests that they have an almost similar density of elastically effective cross-links. Nonetheless, prior studies showed that despite similar moduli, the cross-linker geometry can influence how the mesogens align with the network backbone,[23–25] thereby affirming the significance of the comparison of the opto-mechanical responses for these two types.

2.2 Measurements

The experimental geometry, indicating the stretching direction, helical axis and direction of the incident light, is depicted in Fig. 1c. A strip-shaped specimen with dimensions of 3 mm × 1 mm × 30 μm was incrementally stretched along the x-direction (perpendicular to the helical axis) using a home-built, precision-controlled extensometer. This device ensures symmetric extension from both ends, facilitating continuous observation of the sample's central region throughout the stretching process.

Transmitted light spectra were obtained for both right- (R) and left-handed (L) circularly polarized light aligned with the helical axis. Each spectral measurement was conducted after a five-minute stabilization period under the target strain at 25 °C to ensure the tensile stress reached quasi-equilibrium. A Hamamatsu Photonics PMA12C detector was employed to quantify the light spectra. Illumination was provided by a tungsten lamp, with circular polarization achieved by using circular polarizers.

The strip specimens were progressively extended using an elongation device coupled to an optical microscope. The lateral contraction in the y-direction during uniaxial stretching in the x-direction was examined. The axial ratio λ_y ($\lambda_y = l_y/l_{y0}$ where l_y is the length in the y-direction, and l_{y0} is the initial length) was evaluated as a function of λ_x. The ratio λ_z in the thickness direction was computed from volume conservation ($\lambda_x\lambda_y\lambda_z = 1$) during stretching. The volume constancy was validated by a complementary tensile test by measuring directly the thickness variation using a double-scan high-precision laser measuring instrument Keyence LT-9010M, which will be shown in the later section.

The stress–strain relationships under uniaxial elongation were investigated for a strip-shaped specimen (3 mm × 1 mm × 30 μm) using a tensile tester AC-500N-CM (T.S.E., Japan). The specimens were elongated in the x-direction with a crosshead speed of 0.1 mm s^{-1}. This strain rate was sufficiently slow to observe the quasi-equilibrium stress–strain behavior.

Director reorientation behavior driven by elongation was examined using wide-angle X-ray scattering (WAXS) measurements. The experiments were conducted at the BL-6A beamline of the photon factory of the high energy accelerator research organization (Tsukuba, Ibaraki, Japan) using an imaging plate as the detector. The X-ray wavelength was 0.15 nm, and the sample-to-detector distance was 1.0 m. To intensify the scattering intensity, multiple layers of the sample, composed of four strips each 30 mm × 10 mm × 30 μm, were laminated together. The two-dimensional scattering patterns were sequentially recorded at the central specimen region for various tensile strains, with a waiting period of five minutes after each strain to equilibrate the tensile stress. The specimens were stretched up to a given true-stretching ratio by using a compact tensile testing machine (ISUT-2207; IS Giken Co., Japan) at room temperature. The imaging plate, BAS-IP MS 2025 (Fuji Photo Film Co., Japan; size: 200 × 250 μm^2), has an actual pixel size of 100 × 100 μm^2. The typical exposure time was in the range of 10–30 s. BAS2500 (Fuji Photo Film Co., Japan) was used for the development of exposed images on the imaging plate. A polyethylene crystal was used as the standard sample to calibrate the magnitude of the scattering vector.

For each measurement, the data reproducibility was verified by multiple tests on the same specimens, yielding an error margin within 10%.

3. Results and discussion

Fig. 2 and 3 illustrate the transmission spectra of CLCE-0 and CLCE-4 when exposed to right- (R) and left-handed (L) circularly polarized light. These figures depict the spectral changes as the specimens are stretched along the x-axis by a factor of λ_x. In their initial, undeformed state ($\lambda_x = 1$), both CLCE specimens exhibit selective reflection, characterized by a significant dip of transmittance in a specific wavelength range for R light, due to reflection at these wavelengths. In contrast, L light shows nearly complete transmittance across the entire wavelength range. The central wavelength of the reflection band, Λ_R, is evaluated to be 650 for CLCE-0 and 600 nm for CLCE-4. As λ_x increases, Λ_R shifts toward shorter wavelengths. This trend continues until a saturation point is reached at higher values of λ_x. The spectral shift for CLCE-0 at a stretch of $\lambda_x = 2$ is visually represented by a color transition from red to dark green in the inset of Fig. 2a. Notably, a slight stretch ($\lambda_x = 1.1$) begins to reduce the transmittance for L around Λ_R, indicating a disturbance in the selective reflection. As λ_x further increases, this reduction in L light transmission intensifies, and the specific wavelength for L light (Λ_L) also shifts to shorter wavelengths. At higher elongation, the transmission spectra for R and L

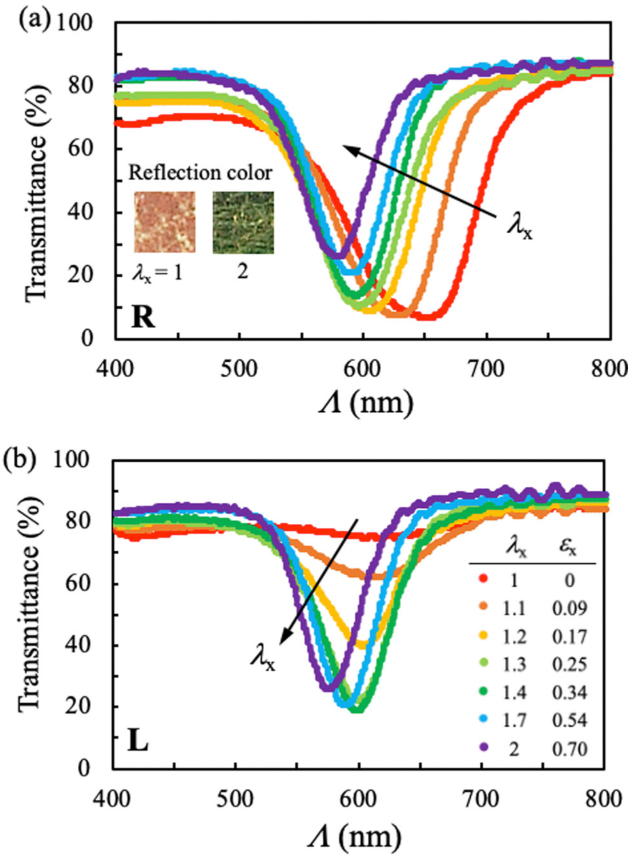

Fig. 2 Transmission spectra of CLCE-0 under uniaxial extension for (a) right- and (b) left-handed circularly polarized incident light as a function of stretch (λ_x) or true strain (ε_x) in the x-direction. The insets in (a) display the change in reflection color after the stretching of $\lambda_x = 2$.

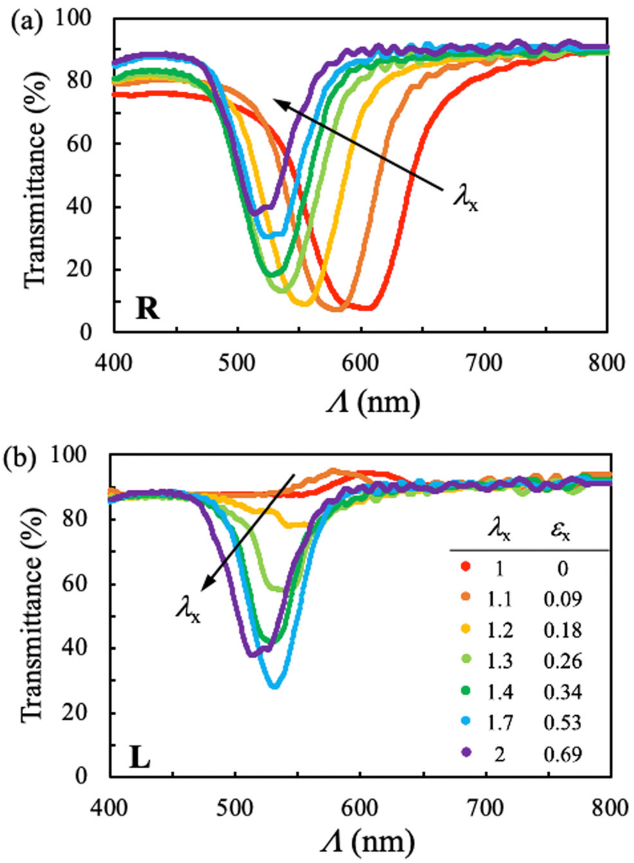

Fig. 3 Transmission spectra of CLCE-4 under uniaxial extension for (a) right- and (b) left-handed circularly polarized incident light as a function of stretch (λ_x) or true strain (ε_x) in the x-direction.

progressively converge, eventually becoming indistinguishable. This convergence is indicative of a complete loss of selective reflection.

The reduction of selectivity under stretching can be attributed to the deformation of the helical structure. The initial uniform helical director configuration undergoes a noticeable distortion by minimal stretching, leading to a reduction of selectivity. The transmittance for L decreases because the distorted helix can no longer efficiently guide this polarization through. Conversely, the transmittance for R increases since the disruption allows light of this polarization, which was previously filtered out, to pass more readily. Further stretching beyond a critical stretch can ultimately destroy the helical structure yet preserving a degree of regularity along the original helical axis. Consequently, although the material loses its selective reflective capabilities, a form of Bragg's reflection persists. The theoretical calculations for the stretching driven structural variation will be discussed later.

Parts a and b of Fig. 4 present the variations in Λ_R and Λ_L, as well as the corresponding absorbance $[\mathrm{Abs}]_R$ and $[\mathrm{Abs}]_L$, for CLCE-0 and CLCE-4, respectively. These values are plotted against the longitudinal true strain ε_x, which is defined as $\varepsilon_x \equiv \ln \lambda_x$. Both CLCE samples exhibit similar qualitative trends in these quantities as a function of ε_x. The behavior of Λ_R, Λ_L and [Abs] can be categorized into three distinct regimes, using the two strain thresholds ε_x' and ε_x''. In region I $\left(\varepsilon_x < \varepsilon_x'\right)$, as ε_x increases, the differences between Λ_R^* and Λ_L^* diminish, indicating a progressive alternation in the original helical director configuration induced by the applied strain. In region II $\left(\varepsilon_x' < \varepsilon_x < \varepsilon_x''\right)$, Λ_R and Λ_L converge and remain constant with respect to ε_x. The disparity in $[\mathrm{Abs}]_R$ and $[\mathrm{Abs}]_L$ progressively diminishes as ε_x approaches ε_x''. In region III $\left(\varepsilon_x > \varepsilon_x''\right)$, with the convergence of Λ and [Abs] between L and R light, the material maintains a periodic structure in the thickness (z-) direction, characterized by Λ. As ε_x increases, there is a slight reduction in Λ. The strain thresholds ε_x' and ε_x'' for both specimens are comparable, with $\varepsilon_x'' \approx 0.53$ for both, while $\varepsilon_x' \approx 0.25$ and 0.30 for CLCE-0 and CLCE-4, respectively. These threshold values demarcate the transition points where the reflection wavelengths and absorbance values for R and L light begin to align and where they nearly converge.

Fig. 5a depicts the two dimensional WAXS patterns of CLCE-0 at various ε_x values when elongated in the x-direction, with the incident X-ray beam aligned parallel to the helical axis (z-axis). The patterns exhibit diffraction at approximately 0.41 nm, characteristic of the spacing between mesogenic groups in nematic liquid crystals.[29] In the undeformed state,

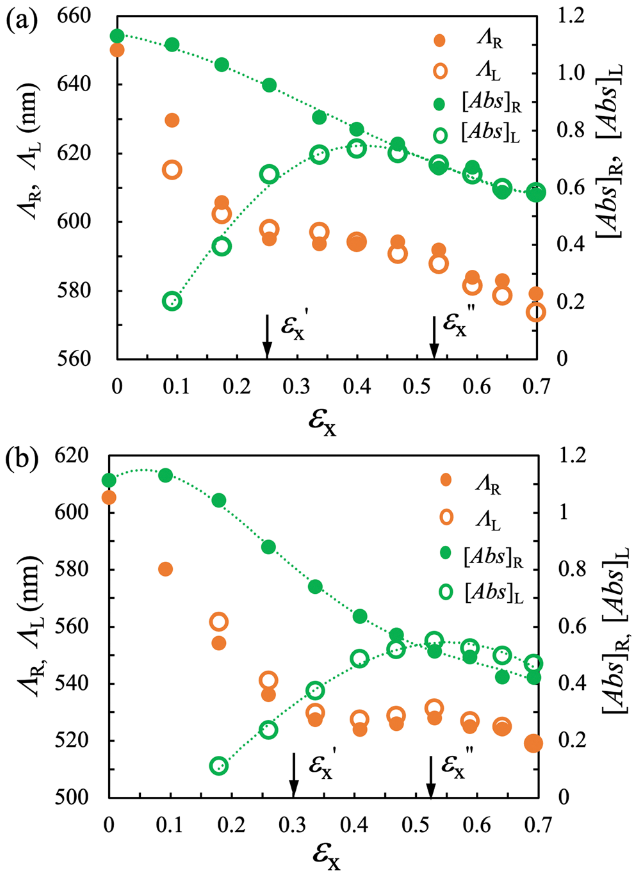

Fig. 4 Characteristic reflection wavelengths (Λ_R for right-handed and Λ_L for left-handed circularly polarized light) and their corresponding absorbance values ($[\text{Abs}]_R$ and $[\text{Abs}]_L$) as a function of tensile true strain in the x-direction (ε_x) for (a) CLCE-0 and (b) CLCE-4. The strains ε_x' and ε_x'' represent the thresholds at which the and values align, and where the $[\text{Abs}]_R$ and $[\text{Abs}]_L$ values converge, respectively.

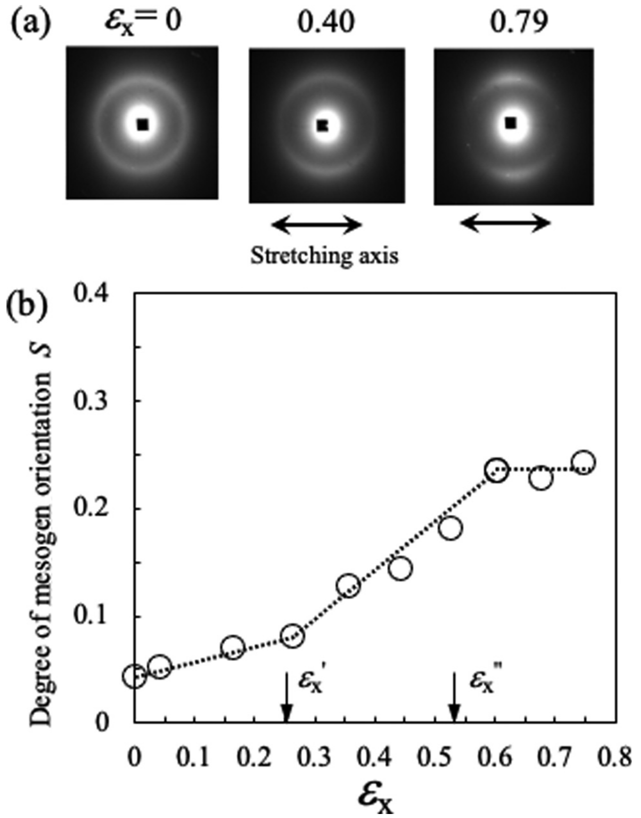

Fig. 5 (a) Two dimensional wide-angle X-ray scattering patterns for CLCE-0 at various ε_x values. (b) Degree of orientation of local directors in the elongation (x) direction as a function of tensile true strain in the x-direction (ε_x) for CLCE-0.

an isotropic diffraction ring is evident, indicative of a random director distribution in the xy-plane. As ε_x increases, the diffraction patterns evolve into arc shapes perpendicular to the elongation direction, signifying an increase in the orientation of directors aligned with the stretch. Fig. 5b shows the degree of mesogen orientation (S) along the x-direction as a function of ε_x. This parameter, derived from the analysis of the scattering intensity distribution,[30] is nearly zero in the undeformed state, reflecting the isotropic director orientation in the xy-plane. Notably, the ε_x dependence of S is classified into three distinct regimes, corresponding to the ε_x' and ε_x'' thresholds determined from the Λ and [Abs] data in Fig. 4. When ε_x increases from zero, S incrementally rises, yet the relationship between S and ε_x undergoes a marked transition near ε_x'. The pronounced change in S within region II is indicative of the predominant rotation of the directors within the xy-plane towards the x-axis. Beyond ε_x'' (in region III), S stabilizes at approximately 0.25, indicating the full alignment of the local directors toward the x-direction.

Fig. 6a and b display the lateral true strains ($\varepsilon_y \equiv \ln \lambda_y$ and $\varepsilon_z \equiv \ln \lambda_z$) as a function of longitudinal true strain (ε_x) for CLCE-0 and CLEC-4, respectively. The strain in the thickness direction (ε_z) is calculated using the incompressibility conditions ($\lambda_x\lambda_y\lambda_z = 1$, *i.e.*, $\varepsilon_x + \varepsilon_y + \varepsilon_z = 0$). This incompressibility under uniaxial stretching has been independently verified by measuring strains in all three directions, which is shown in Fig. 6c. Lateral contractions in the y- and z-directions during uniaxial stretching in the x-direction are quantified by Poisson's ratios μ_{xy} and μ_{xz}, defined as $\varepsilon_y = -\mu_{xy}\varepsilon_x$ and $\varepsilon_z = -\mu_{xz}\varepsilon_x$. In incompressible and isotropic materials such as conventional rubber, these ratios are identical with $\mu_{xy} = \mu_{xz} = 0.5$. In the figures, the slope represents the μ value. For both CLCE-0 and CLCE-4, a pronounced transition in μ values is observed around two specific strain thresholds, ε_x' and ε_x''. In region II, μ_{xz} is substantially lower than μ_{xy}, whereas in regions I and III, they are similar, approximating to 0.5. Notably, in region II for CLCE-0 and CLCE-4, μ_{xz} values are 0.25 and 0, respectively. Specifically, for CLCE-4, $\mu_{xz} = 0$ and $\mu_{xy} = 1$ signify a marked anisotropic deformation pattern, where lateral contraction occurs solely in the y-direction without any dimensional reduction in the z-direction (*i.e.*, along the helical axis). This behavior indicates a unique deformation pattern where the local directors predominantly rotate within the xy-plane, as illustrated in Fig. 5. This significant anisotropic lateral contraction during uniaxial stretching is similar to the response seen in monodomain nematic elastomers when stretched perpendicular to their initial director axis.[31–34] In LCEs, there

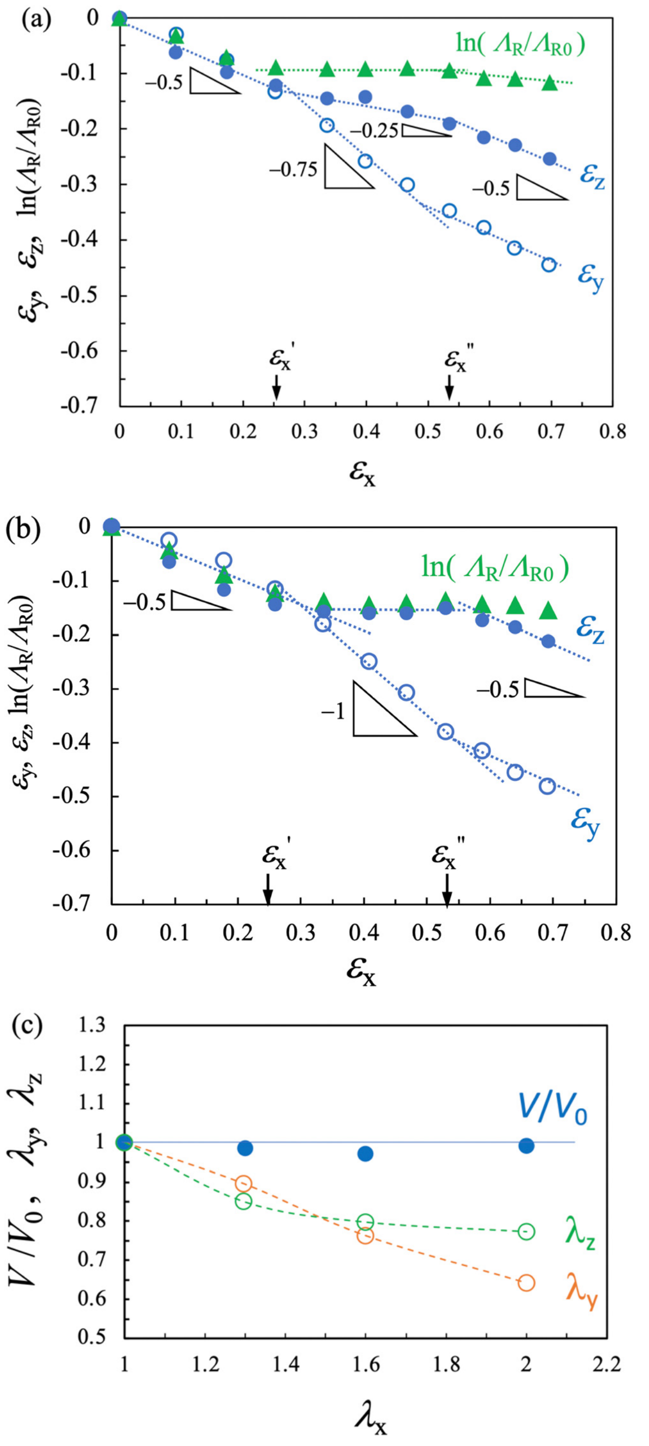

Fig. 6 Lateral true strain in y, z-direction (ε_y and ε_z), and $\ln(\Lambda_R/\Lambda_{R0})$ as a function of longitudinal true strain in x-direction (ε_x) for (a) CLCE-0 and (b) CLCE-4. (c) Changes in dimensions in the y- and z-directions (λ_y and λ_z) and relative volume (V/V_0) as a function of stretch in the x-direction (λ_x) for CLCE-0. The dashed lines are guides for eyes.

is a strong interdependency between the alignment of the liquid crystals and the macroscopic deformation. Therefore, the absence of noticeable deformation along the z-axis ($\mu_{xz} = 0$) can be logically attributed to the director realignment primarily taking place with the xy-plane. As depicted in Fig. 5, in region III, S remains constant with increasing ε_x, indicating that the local directors are fully rotated towards the x-axis. Consequently, macroscopic deformation in this regime resembles that of conventional isotropic rubber, with $\mu_{xy} = \mu_{xz} = 0.5$. In region I, the modest change in S with respect to ε_x suggests that the director realignment toward the x-direction within the xz-plane occurs alongside that within the xy-plane, likely resulting in isotropic lateral contractions.

The compression of the helical director configuration due to uniaxial stretching is characterized by Λ_R/Λ_{R0} where Λ_{R0} is the initial value in the undeformed state. We also plot the corresponding true compressive strain, $\ln(\Lambda_R/\Lambda_{R0})$, as a function of ε_x in Fig. 6a and b. The slope of $\ln(\Lambda_R/\Lambda_{R0})$ exhibits a significant change around ε_x', similar to the change observed for the μ values, albeit the change around ε_x'' is less pronounced. Importantly, the value of Λ_R remains unchanged during stretching for both CLCEs, highlighting a unique correlation with negligible dimensional change along the helical axis in region II as shown in Fig. 6a and b. In particular, CLCE-4 shows no change in ε_z, mirroring the behavior of Λ_R, while CLCE-0 exhibits a slight change in ε_z.

Fig. 7 presents the nominal tensile stress (σ_x) as a function of ε_x. The $\sigma_x - \varepsilon_x$ relationship for each specimen is divided into three regimes, delineated by two strain thresholds, ε_x' and ε_x''. In regime I, both specimens exhibit an initial increase in stress, with the slope corresponding to their initial Young's moduli: 5.8 MPa for CLCE-0 and 4.5 MPa for CLCE-4. Regime II is characterized by a considerably gentler increase in stress, and the quasi-plateau stress is approximately 0.75 MPa for both specimens. Upon entering region III, there is an appreciable increase of stress with further strain. The quasi-plateau stress is attributed to the predominant rotation of local directors within the xy plane in the corresponding strain regime. Many studies of nematic elastomers have shown that stretching-induced director rotation can lead to a plateau in tensile stress due to the coupling of LC alignment and macroscopic stretch.[4] Similar stress plateau behavior was observed in a CLCE[13] and a twisted nematic

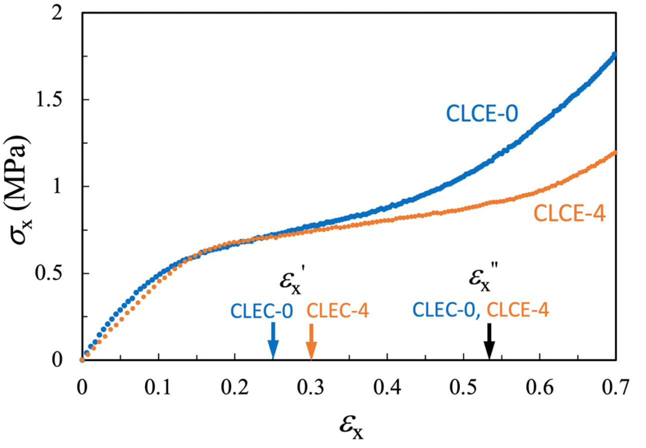

Fig. 7 Quasi-equilibrium nominal stress (σ_x) as a function of tensile true strain in the x-direction (ε_x) for (a) CLCE-0 and (b) CLCE-4.

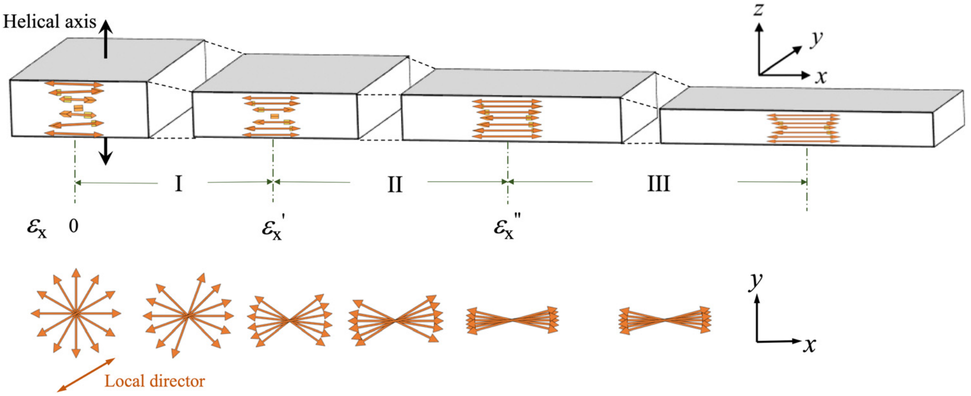

Fig. 8 Schematic diagram of changes in helical director configuration and macroscopic dimensions of CLCE in the three strain regimes (Regions I, II, III) during uniaxial stretching.

elastomer[35] subjected to uniaxial stretching. For CLCE-4, the absence of dimensional change in the *z*-direction ($\mu_{xz} = 0$) signifies a pure director rotation confined to the *xy* plane, aligning with the observed pronounced stress-plateau characteristic.

Fig. 8 shows the schematic of the helical director configuration changes and the macroscopic dimensions of CLCEs during uniaxial stretching. This stretching alters the original helical structure that selectively reflects R light. The progression of this alteration is classified into three distinct phases, delineated by strain values ε_x' and ε_x''. At a mere 10% stretch, the transmission spectra exhibit a noticeable decrease in L light transmission, signaling the onset of helical disruption. In region I $\left(\varepsilon_x < \varepsilon_x'\right)$, there is a gradual realignment of the local directors within both the *xy*- and *xz*-planes toward the *x*-direction. This realignment is accompanied by a decrease in helical pitch proportional to the dimensional reduction along the helical axis. Transitioning to region II $\left(\varepsilon_x' < \varepsilon_x < \varepsilon_x''\right)$, the rotation of directors within the *xy*-plane toward the *x*-direction becomes dominant, leading to the eventual disappearance of reflective selectivity. In this phase, the helical pitch does not change, and there is minimal dimensional reduction along the helical axis. In region III $\left(\varepsilon_x > \varepsilon_x''\right)$, the director orientation stabilizes. The CLCEs behave mechanically like conventional elastomers whereas a periodic structure persists in the *z*-direction. While similar qualitative behaviors are observed in uniaxially stretched CLCEs with various chemical compositions,[6–8,13] this study distinctly categorizes the process into three separate strain regimes defined by two strain thresholds. At each threshold strain, several optical and mechanical properties display definitive crossovers in the strain dependencies. These include the absorbances at characteristic wavelengths, the degree of mesogen orientation in the *xy* plane (S), both Poisson's ratios (μ_{xy} and μ_{xz}) related to macroscopic lateral contractions and microscopic compression of the helical pitch, and the tensile stress.

The opto-mechanical behavior of CLCEs under this stretching geometry was theoretically explored by Warner and coworkers.[26,27,36] In this section, we compare our experimental results for the ε_x dependencies of $\ln(\Lambda_R/\Lambda_{R0})$, μ_{xy}, μ_{xz} (Fig. 6) and tensile stress (Fig. 7) with the model predictions. They derived an expression of the free energy $F(\lambda_x, \lambda_y, r, \Phi, \Phi_0)$ for this system (inset in Fig. 9a) where r represents the polymer

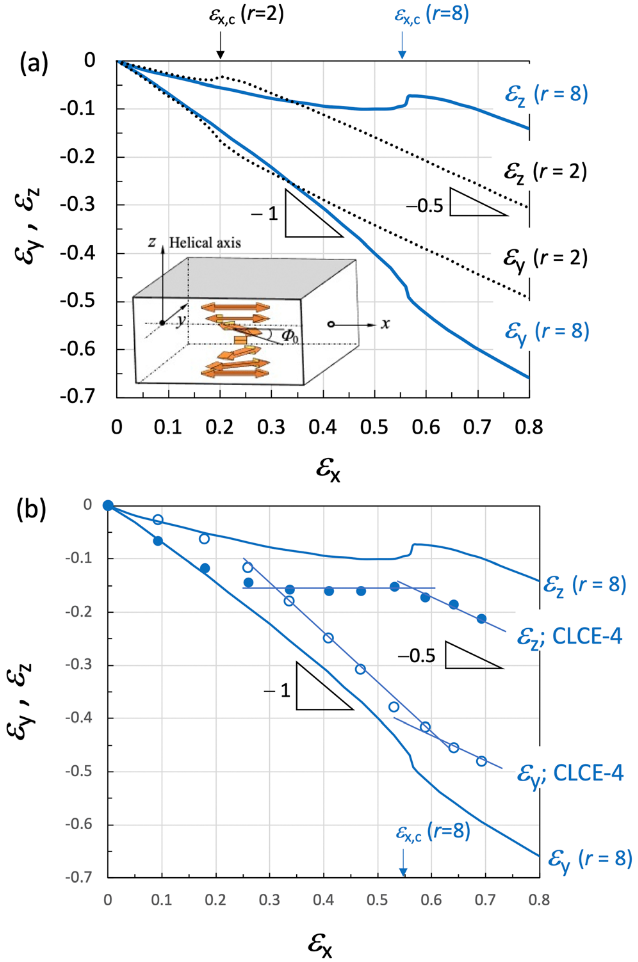

Fig. 9 (a) Initial director angle Φ_0 of a cholesteric helix in the model. Lateral true strains ε_y and ε_z as a function of longitudinal true strain ε_x calculated for r = 8 and 2. The critical strain is $\varepsilon_{x,c} \approx 0.55$ ($\lambda_c \approx 1.73$) or 0.20 ($\lambda_c \approx 1.20$) for r = 8 or 2, respectively. (b) Comparison of the model prediction with r = 8 with the data of CLCE-4 reproduced from Fig. 6b.

network anisotropy, Φ_0 and Φ denote the director angles in the initial and deformed states, respectively.[26,27,36] The free energy function F is expressed as:

$$F=\frac{G}{2}\Bigg\{\lambda_x{}^2+\lambda_y{}^2+\frac{1}{\lambda_x{}^2\lambda_y{}^2}$$
$$+\frac{r-1}{4r}\big[(r-1)\left(\lambda_x{}^2+\lambda_y{}^2\right)(1-\cos 2\Phi_0\cos 2\Phi)$$
$$+(r+1)\left(\lambda_x{}^2-\lambda_y{}^2\right)(\cos 2\Phi_0-\cos 2\Phi)-2(r-1)\lambda_x\lambda_y\sin 2\Phi_0\sin 2\Phi\big]\Bigg\} \quad (1)$$

where G is the shear modulus, and λ_z is obtained from volume conservation during deformation defined by $\lambda_z = 1/(\lambda_x\lambda_y)$. The theory assumes the affine relationship between helical and macroscopic deformations. Minimizing F with respect to Φ provides the variation in the director angle, $\Phi(z)$, with the distance z along the helical axis in response to an applied stretch by λ_x. This variation is expressed by the following equation:[26,27,36]

$$\tan 2\Phi=\frac{2\lambda_x\lambda_y(r-1)\sin 2\Phi_0}{(r-1)\left(\lambda_x{}^2+\lambda_y{}^2\right)\cos 2\Phi_0+(r+1)\left(\lambda_x{}^2-\lambda_y{}^2\right)} \quad (2)$$

The optimal lateral contractions, λ_y and λ_z, are determined by minimizing the total free energy for half a helix repeat with respect to λ_y as[26,27,36]

$$\frac{\pi}{4}\frac{(r+1)^2}{r}-\frac{\pi}{\lambda_y{}^4\lambda_x{}^2}$$
$$-\frac{r-1}{2r}\int_0^{\pi/2}\mathrm{d}\Phi_0\left\{\frac{a_1\left[(r+1)-(r-1)\cos 2\Phi_0\right]-4r\lambda_x{}^2}{\sqrt{a_1{}^2-4r\lambda_x{}^2\lambda_y{}^2}}\right\}=0 \quad (3a)$$

where

$$a_1=\frac{1}{2}\left[(r+1)\left(\lambda_x{}^2+\lambda_y{}^2\right)+(r-1)\left(\lambda_x{}^2-\lambda_y{}^2\right)\cos 2\Phi_0\right] \quad (3b)$$

The numerical solutions for λ_y and λ_z as a function of λ_x for given r values are obtained from eqn (3), with the Φ variation along the helical axis for each λ_x computed from eqn (2) thereafter. These relationships depend on both r and λ_x.

Fig. 10a illustrates the stretch-induced Φ variation for $r = 8$ which is calculated using the numerical solutions for λ_y and λ_z at each λ_x shown in Fig. 9a. Initially, at $\lambda_x = 1$, the ideal helix is represented by a straight line, indicating a linear variation of Φ from 0 to π along z. A small stretch causes a noticeable helix distortion, reducing reflection selectivity as observed in the experiments. Beyond a critical stretch ($\lambda_{x,\mathrm{c}} \approx 1.73$, $\varepsilon_{x,\mathrm{c}} \approx 0.55$), the helix totally loses the chiral nature, and $\Phi(z)$ begins to oscillate around 0. This corresponds to the transition behavior from region II to region III observed experimentally. Even at higher stretch of $\lambda_x = 3$, the structure maintains periodicity, as shown by the finite degree of oscillation around zero. This periodicity is observed as a form of Bragg's reflection in the transmission spectra. The selected r value ($r = 8$) was determined by numerical calculation so that the theoretical strain threshold ($\varepsilon_{x,\mathrm{c}}$) could align with the experimental value of ε_x''. Mao *et al.* derived a relationship of $\lambda_{x,\mathrm{c}} \approx r^{2/7}$ assuming small deformation of $\varepsilon_x \approx 0$,[26,27] but it does not hold for larger experimental ε_x'' values (≈ 0.5) observed in this study. Importantly, the theoretical results for $r = 8$ predict a transition from a significant anisotropic deformation characterized by $\mu_{xz} = \ln(\Lambda_\mathrm{R}/\Lambda_{\mathrm{R}0}) = 0$ and $\mu_{yz} = 1$ to conventional isotropic deformation of $\mu_{xy} = \mu_{xz} = 1/2$ (Fig. 9b), in agreement with the experimental observations for CLCE-4.

The nominal tensile stress $\sigma(\lambda_x)$ is obtained by coarse-graining the derivative of F with respect to λ_x over one turn of the helix as $\int_0^\pi \mathrm{d}\Phi_0(\partial F/\partial\lambda_x)$:

$$\sigma/G = b_1-\frac{b_2}{\lambda_x{}^3\lambda_y{}^3}$$
$$+\frac{r-1}{4r}\int_0^\pi \mathrm{d}\Phi_0\big[b_1(r-1)(1-\cos 2\Phi_0\cos 2\Phi)$$
$$+b_3(r+1)(\cos 2\Phi_0-\cos 2\Phi)-b_2(r-1)\sin 2\Phi_0\sin 2\Phi\big] \quad (4)$$

where $b_1(\lambda_x, \lambda_y) = \lambda_x + \lambda_y(\mathrm{d}\lambda_y/\mathrm{d}\lambda_x)$, $b_2(\lambda_x, \lambda_y) = \lambda_y + \lambda_x(\mathrm{d}\lambda_y/\mathrm{d}\lambda_x)$, and $b_3(\lambda_x, \lambda_y) = \lambda_x - \lambda_y(\mathrm{d}\lambda_y/\mathrm{d}\lambda_x)$. It can be seen in Fig. 11 that the model expects a finite plateau of tensile stress, reflecting a mechanical transition from deformation accompanied by helical distortion to that characteristic of conventional isotropic elastomers. The plateau stress is determined by the Maxwell equal area construction.[27] The stress in the figure is reduced by initial Young's modulus (E) and the theoretical value is obtained by $E = 3G$ for incompressible solids. The reduced stress plateau (σ/E; 0.20), closely matches the experimental result (approximately 0.18 for CLCE-4), as presented in Fig. 11. Nonetheless, the theoretical plateau width is considerably narrower than the experimental observation. This difference can be attributed to the theoretical model assuming a constant director reorientation in the *xy* plane from the beginning of strain application, as shown in the inset of Fig. 9a. In reality, CLCEs have initial orientation fluctuations of local directors in the *xz* plane, affecting the deformation process during the early stretching stage, designated as region I. In the experiments, the linear region with a slope of unity in the σ/E *versus* ε_x plot is evident at $\varepsilon_x < 0.1$, akin to conventional elastomers, while the theoretical line starts with a significantly smaller slope from the onset of strain application due to the director rotation in the *xy* plane. Moreover, the theory expects that the local director pinning at $\Phi = \pi/2$ position breaks down and a discontinuous transition occurs at $\varepsilon_x = \varepsilon_{x,\mathrm{c}}$, as shown in Fig. 10. However, the WAXS diffraction patterns shown in Fig. 5a vary from the isotropic ring to arc shapes that are perpendicular to the stretching direction, without showing distinct diffraction along the stretching direction. This pattern evolution suggests that the stretching driven director reorientation progresses continuously without significant pinning of the director at $\Phi = \pi/2$ position. Consequently, the abrupt changes expected theoretically are not observed experimentally; instead, the experimental result points to a more gradual transition, effectively blurring the expected discontinuities.

The network anisotropy parameter r correlates with the nematic order parameter in the globally aligned state, $S = (r-1)/(r+2)$, yielding $S = 0.7$ for $r = 8$.[27] This is larger than

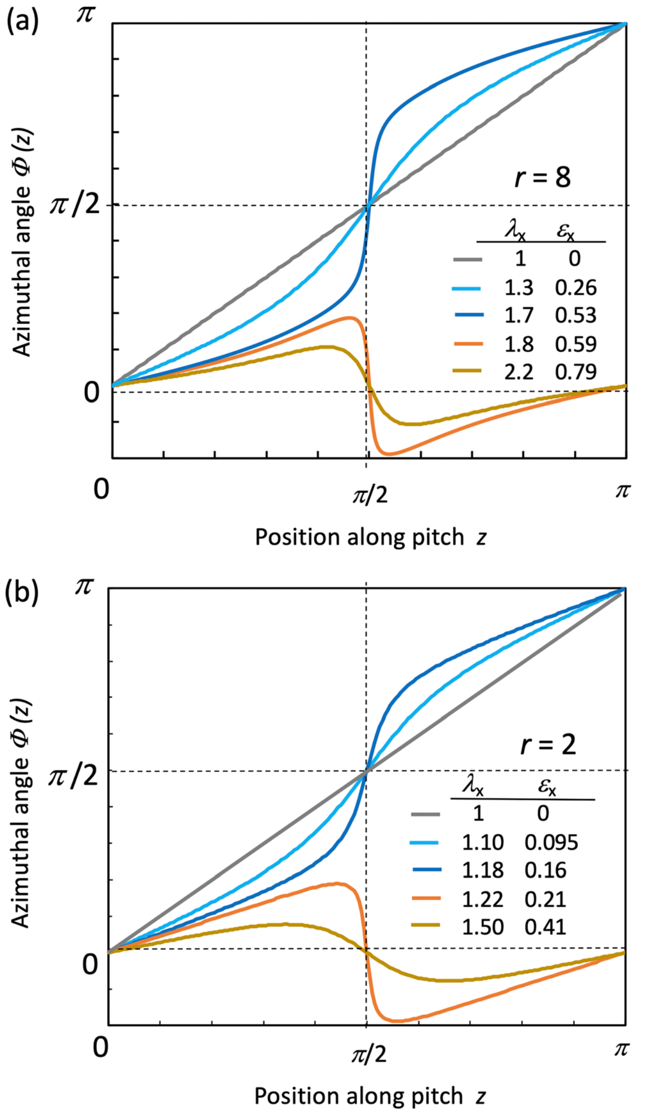

Fig. 10 Director angle Φ as a function of position along pitch z at various degrees of longitudinal true strain (ε_x) calculated for (a) r = 8 and (b)) r = 2. The critical strain is $\varepsilon_{x,c} \approx 0.55$ ($\lambda_{x,c} \approx 1.73$) or 0.20 (($\lambda_{x,c} \approx 1.20$) for r = 8 or 2, respectively.

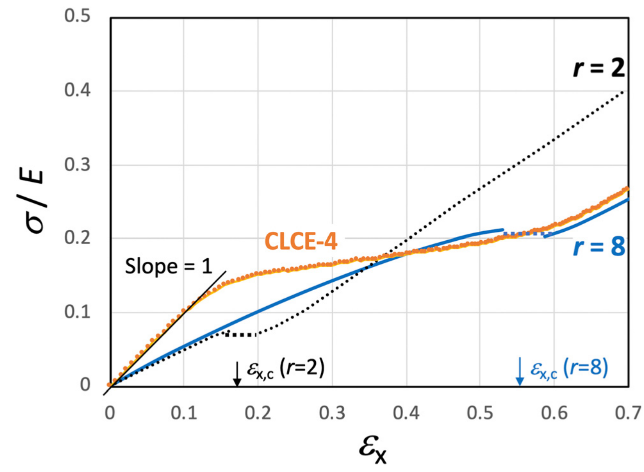

Fig. 11 Nominal tensile stress (σ) reduced by Young's modulus (E) as a function of longitudinal true strain (ε_x) calculated for r = 8 and 2. The critical strain $\varepsilon_{x,c} \approx 0.55$ ($\lambda_{x,c} \approx 1.73$) and 0.20 ($\lambda_{x,c} \approx 1.20$) for r = 8 and 2, respectively. The data of CLCE-4 are reproduced from Fig. 7.

the S value obtained from WAXS measurements ($S_{\mathrm{WAXS}} = 0.25$). However, an r value that corresponds to an S value of 0.25 (r = 2) fails to account for the experimental results. Computations using r = 2 yields a significantly diminished critical strain (approximately 0.2; Fig. 10b), a less anisotropic distortion of the helix ($\mu_{xz} \approx 0.3$; Fig. 9a) and a lower plateau stress (approximately 0.07; Fig. 11). The discrepancy between S = 0.7 for r = 8 and S_{WAXS} values can be attributed to the differences in the degree of mesogen orientation for the network backbone and the total network including elastically inert dangling portions. The main-chain type CLCE specimens under study are expected to contain finite amounts of such dangling portions due to imperfections in the network structure and a side reaction between a thiol and the carbonate group of the chiral molecules.[37] While the WAXS tests capture the entire mesogen orientation including dangling portions, the dangling chains do not contribute to stress-induced distortion of the helical structure, as they are elastically inactive. Davidson *et al.*[35] employed almost the same value of r = 8.5 in this model to explain the opto-mechanical response for a twisted nematic elastomer with an almost similar structure to the CLCEs in this study.

Summary

We investigate the opto-mechanical behavior of two CLCE films, referred to as CLCE-0 and CLCE-4 with or without an explicit tetra-functional cross-linker, respectively, under uniaxial stretching perpendicular to the initial helical axis (z-axis).

Stretching along the x-axis causes a blue shift of the characteristic reflection band, as a result of helical pitch reductions accompanied by initial disruption of helical director configurations. Notably, beyond a certain strain threshold (ε_x'), the helical pitch ceases to change in both CLCEs. Correspondingly, macroscopic lateral contractions become markedly anisotropic, particularly in CLCE-4, where the contraction along the helical axis is absent, characterized by a Poisson's ratio (μ_{xz}) of zero. CLCE-0 undergoes less anisotropic contractions, with $\mu_{xz} \approx 0.25$, which aligns with prior studies[23–25] that highlighted the appreciable influence of the cross-linker geometry on the coupling between mesogen alignment and macroscopic deformation. In this intermediate strain regime, the rotation of local directors toward the x-direction occurs predominantly in the xy-plane, accompanied by a quasi-plateau stress. In the higher end of this strain regime (ε_x''), the transmission spectra for right- and left-handed circularly polarized light become almost identical, indicative of the total loss of reflection selectivity. In higher strain regions, the mechanical behaviors of both CLCEs align with isotropic conventional rubbers, yet they retain a periodic structure capable of Bragg reflection without selectivity for circular polarization of light. The key features of the observations align with the Mao–Terentjev–Warner model predictions when the network anisotropy parameter (r) is tailored in line with the observed critical strain $\left(\varepsilon_x''\right)$ for the total loss of reflection selectivity.

These findings enhance our comprehension of the intricate interplay between the liquid crystal alignment and mechanical strain in CLCEs. These insights provide a basis for future explorations into the opto-mechanical and mechanochromic properties of CLCEs under diverse deformations toward their innovative applications in smart materials and adaptive optics.

Conflicts of interest

There are no conflicts to declare.

Acknowledgements

The authors appreciate BASF, Japan and Osaka Organic Chemical Industry Ltd. for the provision of LC756 and RM-82, respectively. This work is partly supported by JSPS KAKENHI Grant No. 22H02143.

References

1 P. Oswald and P. Pieranski, *Nematic and Cholesteric Liquid Crystals*, ed. G. W. Gray, J. W. Goodby and A. Fukuda, CRC Press, Boca Raton, 2005.

2 P. G. de Gennes and J. Prost, *The Physics of Liquid Crystals*, Oxford University Press, New York, 2nd edn, 1993.

3 S. T. Kim and H. Finkelmann, Cholesteric Liquid Single-Crystal Elastomers (LSCE) Obtained by the Anisotropic Deswelling Method, *Macromol. Rapid Commun.*, 2001, **22**(6), 429–433.

4 M. Warner and E. M. Terentjev, *Liquid Crystals Elastomers*, Clarendon Press, London, 2003.

5 H. Finkelmann, S. T. Kim, A. Munoz, P. Palffy-Muhoray and B. Taheri, Tunable Mirrorless Lasing in Cholesteric Liquid Crystalline Elastomers, *Adv. Mater.*, 2001, **13**(14), 1069–1072.

6 P. Cicuta, A. R. Tajbakhsh and E. M. Terentjev, Evolution of Photonic Structure on Deformation of Cholesteric Elastomers, *Phys. Rev. E: Stat., Nonlinear, Soft Matter Phys.*, 2002, **65**(5), 51704.

7 P. Cicuta, A. R. Tajbakhsh and E. M. Terentjev, Photonic Gaps in Cholesteric Elastomers under Deformation, *Phys. Rev. E: Stat., Nonlinear, Soft Matter Phys.*, 2004, **70**(1), 11703.

8 C. Bourgerette, B. Chen, H. Finkelmann, M. Mitov, J. Schmidtke and W. Stille, Variation of the Network Anisotropy of Cholesteric Side Chain Elastomers, *Macromolecules*, 2006, **39**(23), 8163–8170.

9 H. Nagai and K. Urayama, Thermal Response of Cholesteric Liquid Crystal Elastomers, *Phys. Rev. E: Stat., Nonlinear, Soft Matter Phys.*, 2015, **92**(2), 022501.

10 M. T. Brannum, A. M. Steele, M. C. Venetos, L. T. J. Korley, G. E. Wnek and T. J. White, Light Control with Liquid Crystalline Elastomers, *Adv. Opt. Mater.*, 2019, **7**(6), 1801683.

11 Y. Fuchigami, T. Takigawa and K. Urayama, Electrical Actuation of Cholesteric Liquid Crystal Gels, *ACS Macro Lett.*, 2014, **3**(8), 813–818.

12 A. M. Menzel and H. R. Brand, Cholesteric Elastomers in External Mechanical and Electric Fields, *Phys. Rev. E: Stat., Nonlinear, Soft Matter Phys.*, 2007, **75**(1), 11707.

13 R. Kizhakidathazhath, Y. Geng, V. S. R. Jampani, C. Charni, A. Sharma and J. P. F. Lagerwall, Facile Anisotropic Deswelling Method for Realizing Large-Area Cholesteric Liquid Crystal Elastomers with Uniform Structural Color and Broad-Range Mechanochromic Response, *Adv. Funct. Mater.*, 2020, **30**(7), 1909537.

14 Y. Geng, R. Kizhakidathazhath and J. P. F. Lagerwall, Robust Cholesteric Liquid Crystal Elastomer Fibres for Mechanochromic Textiles, *Nat. Mater.*, 2022, **21**(12), 1441–1447.

15 A. Varanytsia, H. Nagai, K. Urayama and P. Palffy-Muhoray, Tunable Lasing in Cholesteric Liquid Crystal Elastomers with Accurate Measurements of Strain, *Sci. Rep.*, 2015, **5**, 17739.

16 J. Schmidtke, S. Kniesel and H. Finkelmann, Probing the Photonic Properties of a Cholesteric Elastomer under Biaxial Stress, *Macromolecules*, 2005, **38**(4), 1357–1363.

17 F. Serra, M. A. Matranga, Y. Ji and E. M. Terentjev, Single-Mode Laser Tuning from Cholesteric Elastomers Using a "Notch" Band-Gap Configuration, *Opt. Express*, 2010, **18**(2), 575–581.

18 Y. Hirota, Y. Ji, F. Serra, A. R. Tajbakhsh and E. M. Terentjev, Effect of Crosslinking on the Photonic Bandgap in Deformable Cholesteric Elastomers, *Opt. Express*, 2008, **16**(8), 5320–5331.

19 O. T. Picot, M. Dai, E. Billoti, D. J. Broer, T. Peijs and C. W. M. Bastiaansen, A Real Time Optical Strain Sensor Based on a Cholesteric Liquid Crystal Network, *RSC Adv.*, 2013, **3**(41), 18794–18798.

20 P. Zhang, X. Shi, A. P. H. J. Schenning, G. Zhou and L. T. de Haan, A Patterned Mechanochromic Photonic Polymer for Reversible Image Reveal, *Adv. Mater. Interfaces*, 2020, **7**(3), 1901878.

21 M. Kishino, N. Akamatsu, R. Taguchi, K. Hisano, K. Kuwahara, O. Tsutsumi, J. Takeya and A. Shishido, Neutral Mechanical Plane Shifting in Bending Elastomer Film Revealed by Quantification of Internal Strain, *Adv. Eng. Mater.*, 2022, **24**(6), 2101041.

22 A. M. Martinez, M. K. McBride, T. J. White and C. N. Bowman, Reconfigurable and Spatially Programmable Chameleon Skin-Like Material Utilizing Light Responsive Covalent Adaptable Cholesteric Liquid Crystal Elastomers, *Adv. Funct. Mater.*, 2020, **30**(35), 2003150.

23 S. M. Clarke, A. Hotta, A. R. Tajbakhsh and E. M. Terentjev, Effect of Cross-Linker Geometry on Equilibrium Thermal and Mechanical Properties of Nematic Elastomers, *Phys. Rev. E*, 2001, **64**(6), 61702.

24 A. Tsuchitani, H. Ashida and K. Urayama, Pronounced Effects of Cross-Linker Geometries on the Orientation Coupling between Dangling Mesogens and Network Backbones in Side-Chain Type Liquid Crystal Elastomers, *Polymer*, 2015, **61**, 29–35.

25 M. O. Saed, A. H. Torbati, C. A. Starr, R. Visvanathan, N. A. Clark and C. M. Yakacki, Thiol-Acrylate Main-Chain

Liquid-Crystalline Elastomers with Tunable Thermomechanical Properties and Actuation Strain, *J. Polym. Sci., Part B: Polym. Phys.*, 2017, **55**(2), 157–168.

26 M. Warner, E. M. Terentjev, R. B. Meyer and Y. Mao, Untwisting of a Cholesteric Elastomer by a Mechanical Field, *Phys. Rev. Lett.*, 2000, **85**(11), 2320–2323.

27 Y. Mao, E. M. Terentjev and M. Warner, Cholesteric Elastomers: Deformable Photonic Solids, *Phys. Rev. E: Stat., Nonlinear, Soft Matter Phys.*, 2001, **64**(4 Pt 1), 41803.

28 C. M. Yakacki, M. Saed, D. P. Nair, T. Gong, S. M. Reed and C. N. Bowman, Tailorable and Programmable Liquid-Crystalline Elastomers Using a Two-Stage Thiol-Acrylate Reaction, *RSC Adv.*, 2015, **5**(25), 18997–19001.

29 A. J. Leadbetter and A. I. Mehta, Molecular Packing in the Nematic Phase of Cyano Compounds with Different Ring Systems, *Mol. Cryst. Liq. Cryst.*, 1981, **72**(2–3), 51–57.

30 S. Sakurai, S. Aida, S. Okamoto, T. Ono, K. Imaizumi and S. Nomura, Preferential Orientation of Lamellar Microdomains Induced by Uniaxial Stretching of Cross-Linked Polystyrene-Block-Polybutadiene-Block-Polystyrene Triblock Copolymer, *Macromolecules*, 2001, **34**(11), 3672–3678.

31 P. M. S. Roberts, G. R. Mitchell and F. J. Davis, A Single Director Switching Mode for Monodomain Liquid Crystal Elastomers, *J. Phys. II*, 1997, **7**(10), 1337–1351.

32 K. Urayama, R. Mashita, I. Kobayashi and T. Takigawa, Stretching-Induced Director Rotation in Thin Films of Liquid Crystal Elastomers with Homeotropic Alignment, *Macromolecules*, 2007, **40**(21), 7665–7670.

33 H. Higaki, K. Urayama and T. Takigawa, Memory and Development of Textures of Polydomain Nematic Elastomers, *Macromol. Chem. Phys.*, 2012, **213**(18), 1907–1912.

34 S. Okamoto, S. Sakurai and K. Urayama, Effect of Stretching Angle on the Stress Plateau Behavior of Main-Chain Liquid Crystal Elastomers, *Soft Matter*, 2021, **17**(11), 3128–3136.

35 Z. S. Davidson, N. Kapernaum, J. Fiene, F. Giesselmann and M. Sitti, Twisting and Untwisting of Twisted Nematic Elastomers, *Phys. Rev. Mater.*, 2020, **4**(10), 105601.

36 P. A. Bermel and M. Warner, Photonic Band Structure of Cholesteric Elastomers, *Phys. Rev. E*, 2002, **65**(5), 56614.

37 T. Wang, H. Deng, H. Zeng, J. Shen, F. Xie and C. Zhang, Self-Blowing Non-Isocyanate Polyurethane Foams from Cyclic Carbonate Linseed Oil, *ACS Sustainable Resour. Manag*, 2024, **1**(3), 462–470.